Exploring Adsorption Behavior of Sulfur and Nitrogen Compounds on Transition Metal-Doped Cu (100) Surfaces: Insights from DFT and MD Simulations

Achraf Benbella, Hicham Jabraoui, Imane Matrane, M'Hamed Mazroui

Cite this: DOI: 00.0000/xxxxxxxxxx

Exploring Adsorption Behavior of Sulfur and Nitrogen Compounds on Transition Metal-Doped Cu (100) Surfaces: Insights from DFT and MD Simulations

Achraf Benbella*[a], Hicham Jabraoui*[b], Imane Matrane[a], and M'hammed Mazroui[a]

Received Date
Accepted Date

DOI: 00.0000/xxxxxxxxxx

We conducted an extensive investigation using density functional theory (DFT) calculations and ReaxFF molecular dynamics (MD) simulations to elucidate the mechanisms of desulfurization and denitrogenation on Cu (100) surfaces. This study encompassed both pristine surfaces and those modified with Pt or Rh transition metals. Our primary objective was to gain a deep understanding of the adsorption behavior of thiophene (C_4H_4S) and pyridine (C_5H_5N) molecules on stepped Cu (100) surfaces, which serve as models for sulfur and nitrogen compounds. We systematically explored the interplay among water, adsorption efficiency, and surface regeneration capabilities. Using DFT, we thoroughly examined various aspects, including interaction energies, charge transfers, changes in electron density, and alterations in work function upon molecule adsorption. Notably, we observed a decrease in the interaction energy of thiophene, whereas that of pyridine increased when adsorbed on Pt/Rh-doped surfaces compared to pristine ones. Thiophene adsorption reduced the work function, potentially enhancing detectability, without causing inhibitory effects on any surface. Stepped Cu (100) surfaces demonstrated a strong affinity for thiophene, exhibiting an energy difference of approximately 86 kJ/mol. However, this trend reversed on doped surfaces, where pyridine displayed stronger adsorption than thiophene, resulting in energy differences of around 123 kJ/mol and 62 kJ/mol on Pt-Cu and Rh-Cu surfaces, respectively. Moreover, our investigation highlighted the regeneration capacity of these surfaces, indicating that all surfaces can be considered promising candidates for desulfurization, while only Cu and Pt-Cu surfaces were found to be suitable for denitrogenation. Furthermore, results from MD simulations in combination with Potential of Mean Force (PMF) simulations at 300 K, aligned with DFT calculations, confirmed the adsorption configurations of pyridine and thiophene. This analysis demonstrated the competitive advantage of thiophene over pyridine in adsorption and highlighted the inhibitory effect of water on pyridine adsorption on the Cu (100) surface.

1 Introduction

Environmental protection societies have been advocating for the production of clean fuels with low sulfur content not exceeding 0.1 to 0.2 ppm in diesel and gasoline fuels[1]. This is crucial because sulfur compounds in transportation fuels poison catalysts during the reduction of CO and NO_x[1,2], leading to the production of acid rain and toxic SO_x compounds during fuel combustion. Various methods, such as oxidative desulfurization (ODS)[3], extractive desulfurization (EDS), reactive adsorption desulfurization (RADS), hydrodesulfurization (HDS), and adsorptive desulfurization (ADS), are employed for fuel desulfurization. While HDS is a major process in removing sulfur elements from sulfides, thiols, and thiophene compounds, it is ineffective against the dibenzothiophene (DBT) molecule

* Corresponding authors
[a] Laboratoire de Physique de la Matière Condensée, Faculté des Sciences Ben M'sik, Hassan II University of Casablanca, Casablanca B.P. 7955, Morocco; E-mail: achf1995@gmail.com
[b] LAAS-CNRS, University of Toulouse, 31077 Toulouse, France; E-mail: hicham.jabraoui@laas.fr & hicham.jabraoui@gmail.com
† Electronic Supplementary Information (ESI) available: [The details of the supplementary information are available].

and its derivatives, which are prevalent in diesel fuels[4]. DBT molecules are particularly refractory to HDS treatment, often producing H_2S that limits effective hydrodesulfurization. The reactivity of sulfur compounds increases in the order: thiophene < thiols < sulfides < disulfides, with thiophene being the most challenging element to desulfurize[5]. Adsorption techniques like adsorptive desulfurization (ADS) have shown promise in selectively removing sulfur compounds, especially thiophene, to produce ultra-clean fuel under ambient conditions[5–9]. This efficacy arises from the development of sorbents with higher selectivity for thiophene than other fuel components. However, competitive adsorption with other aromatics must be considered, as it could hinder the desulfurization process. Nitrogen compounds are abundant in gasoline and transport fuels, negatively impacting thiophene adsorption and desulfurization[10]. Pre-removal of nitrogen compounds from fuels through adsorption proves effective in activating desulfurization and producing ultra-clean fuels[11]. Furthermore, excellent adsorbents should exhibit large adsorption capacity and effective regeneration[8,9,12–15].

The quest for materials with high affinity for adsorbing sulfur and nitrogen compounds is also driven by their potential use in fuel cell applications[6,16]. Recent research focuses on sorbents like activated alumina[14,17], zeolite formulations[18,19], and metal-based materials[14,20,21]. Noble metal incorporation (e.g., Pt, Cu, Rh, Pd) enhances catalytic capacity for thiophene/pyridine removal, enabling deep desulfurization/denitrogenation processes[5]. These doped sorbents utilize π-complexation for thiophene and pyridine elimination from liquid fuels[9,22]. Strong bonds are formed through π-complexation between DBT compounds and transition metals due to their electron donation/back-donation capacity. Copper (Cu) has the necessary electronic structure for strong π-complexation, offering high selectivity for thiophene, as demonstrated with Cu(I)Y and Cu(II)Y zeolite formulations[23].

Continued research aims to identify sorbents with high adsorption efficiency for sulfur and nitrogen-containing molecules, free from water-inhibiting effects, and with high regeneration capacity. These criteria guide the selection of sorbents for desulfurization and denitrogenation processes[24]. Previous studies[25–27] highlight efficient π-complexation between thiophene/pyridine and transition metals. Thus, selective adsorption of these molecules on transition metals appears promising due to robust π-complexation interactions. Experimental observations indicate toluene[28,29] and benzene[30] adsorptions limiting thiophene adsorption on HY zeolite, while Cu(I)Y, Cu(II)Y, Ag(I)Y, and Zn(II)Y metal-Y zeolite formulations exhibit strong thiophene selectivity[23]. Transition metal-based surfaces hold potential for adsorbing organic molecules[31–34].

Adsorption on metal surfaces has been extensively studied for its technological relevance in selective adsorption and gas sensing[35,36]. Perfect metallic transition surfaces have been well-researched[25,37–41], but the role of defects (e.g., steps[42,43], vacancies[43], adatoms[44]) in practical applications has been understudied despite their prevalence and superior adsorption compared to flat terraces. Defective surfaces can enhance the interaction of organic molecules, offering potential for efficient gas sensors and sorbent materials[42,43].

Understanding the adsorption of sulfur and nitrogen-containing aromatic molecules on defective metal surfaces at atomic and electronic levels is crucial for designing new sorbents for deep desulfurization and denitrogenation processes. In this study, we investigate the adsorption of thiophene (C_4H_4S) and pyridine (C_5H_5N) on a stepped Cu (100) surface. This surface consists of upper and lower terraces formed by removing atoms along successive dense rows of the ideal structure. We employ density functional theory (DFT) with dispersion corrections and ReaxFF molecular dynamics (MD) to study the individual and mixed adsorption of pyridine and thiophene on Cu (100), considering the inhibiting effect of water and the Cu (100) doping with Pt and Ru for desulfurization and denitrogenation. The combination of DFT and ReaxFF provides insights into reactivity and adsorption mechanisms[45–53]. We analyze total interaction energies, partial radial distribution functions (RDF), statistical investigations, charge transfer, charge density differences, and changes in work function to elucidate the adsorption mechanisms on the studied surfaces.

2 Computational details

2.1 Density Functional Theory

In this study, DFT calculations are performed using the Vienna *ab initio* simulation package (VASP)[54,55]. Herein, the electron-ionic core interaction has been described by the projected augmented wave (PAW) method[56,57]. The exchange-correlation interactions were treated using the Perdew–Burke–Ernzerhof (PBE) formulation of generalized gradient approximation (GGA)[58]. The ionic relaxation was performed using the conjugate gradient method. Taking into account van der Waals interactions in our calcula-

tions, the semi-empirical scheme D2 developed by Grimme is used. The cutoff energy for the plane-wave basis expansion is set to 450 eV, and the K-point is adjusted at 6×6×1 for integration of the Brillouin zone. Spin polarization was taken into account in all calculations as Cu surfaces reveal the magnetic performance[59]. All structures are fully optimized until the total energy converges to 1.0 10^{-6} eV and the force on each atom is smaller than 0.02 eV/ Å.

Our simulation process began with the construction of a realistic Cu supercell based on the anatase crystal structure. This supercell adopted a simple cubic unit cell with lattice parameters a = b = c = 3.62 Å and angles $\alpha = \beta = \gamma = 90^{\circ}$, and was assigned the space group $Fm\bar{3}m$. The surface was modelled by a (4×4) lateral supercell of copper with a slab of five layers of Cu (100) surface. Noteworthy, the bottom two layers of our slabs are fixed at their mass positions, while the ions of the top three layers are allowed to relax to their optimal positions. The vacuum height between neighboring slabs in the direction perpendicular to the surface is maintained at 20 Å, which is sufficient to avoid interactions between adjacent supercells (periodic image) and ignored dipole corrections. The adsorption of thiophene or pyridine is carried out on the perfect and stepped Cu (100) surfaces. The stepped Cu (100) surface was created by removing two rows of Cu atoms from the top layer of the (100) surface, as shown in **Figure 1**b. Further, before commencing the adsorption of the molecules on the defected surfaces, we conducted a thorough geometric re-optimization of this surface, including the relaxation of the atomic positions, the shape and volume of the cells. The fully-optimized geometry are illustrated in **Figure 1**-b. Hence, several possible adsorption configurations for thiophene and pyridine on the stepped Cu (100) surface are also tested, see **Figures** S1 and S2.

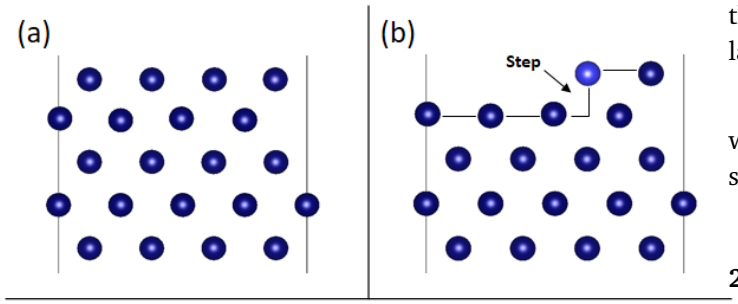

Fig. 1 Side view of simulation cells used in the calculations of Cu (100) surface: (a) perfect surface, and (b) stepped surface. The stepped copper atoms shaded brighter.

To assess the adsorption of pyridine and thiophene molecules adsorbed onto clean and doped Cu (100) stepped surfaces, we calculate the total interaction energy (E_{int}) as follows[60,61]:

$$E_{int} = (E_{mol} + E_{slab}) - E_{sys} \quad (1)$$

where E_{mol}, E_{slab}, and E_{sys} represent the energies of an isolated gas molecule, isolated clean/doped surfaces, and the whole system in interactions 'molecule-surface', respectively. The redistribution of charge upon adsorption on stepped surfaces is known to influence strongly its physical-surface properties, such as its electron density difference and work function change. To investigate this point, we study the difference in electron density ($\Delta\rho$) to further improve our understanding of the adsorption of the two molecules onto the considered Cu, Pt-Cu and Rh-Cu stepped surfaces. To visualize the electron density difference ($\Delta\rho$) introduced by the adsorption of both molecules, we combine the three electron densities: the density of the whole system ($\rho_{\text{molecule}-\text{surface}}$); the density of the isolated molecule (ρ_{molecule}); and the density of the isolated surface (ρ_{surface}) which is formulated as follows[62–64]:

$$\Delta\rho = \rho_{molecule-surface} - \rho_{molecule} - \rho_{surface} \quad (2)$$

Otherwise, the work function could be influenced by the crystallographic orientation and the density of steps and tuned by the adsorption of organic molecules[65]. Thus, we calculated the change in the work function of the stepped surfaces. The work function ϕ is the minimum energy required to displace an electron from the metal surface to the vacuum, which is defined as:

$$\phi = V_{vaccum} - E_{Fermi} \quad (3)$$

where V_{vaccum} is the electrostatic potential in the vacuum region and E_{Fermi} is the Fermi energy. Then, we calculate the work function change ($\Delta\phi$), using the following formulation:

$$\Delta\phi = \phi - \phi_0 \quad (4)$$

where ϕ and ϕ_0 denote the work function of the adsorbed system and the isolated Cu (100) surface, respectively.

2.2 Molecular Dynamics Investigations

In this study, we employed MD simulations within a periodic boundary framework, conducted using the LAMMPS package[66]. Temperature thermalization was achieved using the Nosé-Hoover thermostat. The interactions within the entire system, including Cu−pyridine, Cu−thiophene, Cu−(pyridine thiophene mixing), and Cu−(pyridine thiophene mixing with water), were modeled using the ReaxFF

force field parameters. These parameters were specifically developed to investigate the adsorption and reactivity of systems containing carbon (C), hydrogen (H), nitrogen (N), sulfur (S), and copper (Cu) surfaces[52,67].

The MD simulations of the Cu (100) surface have dimensions of 20.35 Å × 20.35 Å and a height of approximately 27 Å, employing the same Cu-unit cell and (100) surface configuration as used in the DFT calculations. This MD simulation box consists of 288 Cu atoms (see **Figure S5**). Initially, we relaxed the perfect surface alone for 0.1 nanoseconds (ns), with a time step of 1 femtosecond (fs). Subsequently, an additional 0.1 ns relaxation session was performed at 300 K. During this phase, a vacuum was introduced perpendicular to the (100) plane, creating a step defect similar to the previous process. This configuration resulted in a vacuum gap of about 20 Å between two of these relaxed slabs within the periodicity along the z-axis (see **Figure** 1). Our choice to represent Cu through the (100) plane was guided by its unique affinity and propensity for adsorption, particularly involving molecules like water, pyridine, and thiophene[68,69].

Our analysis comprehensively explored the interfacial interactions of thiophene and pyridine with the Cu surface, including water. We focused on interfaces involving pyridine and the Cu(100) surface, thiophene and the Cu(100) surface, as well as the combination of pyridine and thiophene with the Cu(100) surface. Additionally, we delved into the intricate interplay of 20 water molecules at the interface of a mixture of pyridine and thiophene with Cu (100). This investigation involved introducing 12 pyridine molecules (see **Figure 8(b, d)**) and 12 thiophene molecules (depicted in **Figure 8(a, c)**). The balanced composition featuring pyridine and thiophene molecules on the Cu surface is illustrated in **Figure S5**. These interfaces were annealed at 300 K within the NVT ensemble, over 1 ns using a 0.1 fs time step, providing insights into the dynamic behavior of these interfaces.

We also conducted Potential of Mean Force (PMF) calculations using the Steered Molecular Dynamics (SMD) algorithm, which we implemented through the LAMMPS software package[70–73]. Within this computational framework, we imposed a constant negative velocity on one of the atoms from either the thiophene or pyridine molecules participating in the chemical reaction. This method was devised to facilitate the adsorption pathway from the gas phase to the Cu (100) surface.

3 Results

3.1 Density Functional Theory (DFT) Analysis

Thiophene and pyridine adsorption was initiated as a model system on a perfect Cu (100) surface as depicted in **Figure 1-a**. As the presence of defects on any considered surface is unavoidable, we also consider the adsorption on the stepped surface as defective. The defect (**Figure 1-b**) was created by omitting two rows of atoms across the y-direction in the top layer. In order to determine the most stable adsorption configuration, our study was initiated by calculating the total interaction energies of several configurations of two molecules, namely upper terrace, vertical-lower terrace, flat-lower terrace, step, and inclined configurations, on stepped Cu (100) surfaces. All these adsorption configurations are reported in **Figures** S1 and S2 (supplementary material). Furthermore, we studied a substituted Cu (100) stepped surface, where the Cu atoms in the step have been replaced by Pt or Rh atoms. Besides, the adsorption heights S —— Cu and N —— Cu, the carbon-carbon (C —— C) bond distances, and the tilt angle between the molecule plane and the surface plane θ are studied for different defective surfaces of Cu (100), then compared with those of a prefect one.

3.1.1 Adsorption of thiophene

The stepped surface was examined to investigate the influence of defects with weakly coordinated atoms on the surface stability and adsorption behaviour of thiophene. Five different adsorption configurations for thiophene were first tested (**Figure S1**) to define the most stable one. Here, the flat-lower terrace thiophene configuration was found to be the most stable (see **Figure 2**). **Table 1** presents the results of thiophene adsorbed on different considered surfaces of Cu (100) surface.

For a perfect surface, the Hollow-45° site represents the most stable site, with a total interaction energy of 105.16 kJ/mol. The presence of a stepped defect significantly alters the adsorption mechanism of the thiophene molecule while the adsorption order of configuration is found as follows: f-upper terrace < vertical-lower terrace = flat-step < inclined < flat-lower terrace. The flat-lower terrace, like most configuration energies, presents a total interaction energy of 231.565 kJ/mol, higher than for the perfect surface by about 126 kJ/mol. In the same context, a previous simulation study revealed two modes of adsorption for 4,6-dimethyldibenzothiophene (4,6-DMDBT) on MoS_2 surface[5], the flat adsorption via π-interaction and

Table 1 Geometries and total interaction energies (E_{int}) of the relaxed thiophene (C_4H_4S) adsorbed structures on perfect, stepped, and substituted Cu (100) Surface with Pt and Rh atoms.

Sorbent	Adsorption site	E_{int} (C_4H_4S) (kJ/mol)	*S-Cu* (Å)	*C-C*[a] (Å)	θ[b] (deg)
Perfect	Hollow	105.169	2.33	1.38	2
Stepped	f-upper terrace	205.514	2.29	1.38	2
	v-lower terrace	212.268	2.42	1.38	36
	f-lower terrace	231.565	2.40	1.38	22
	f-step	212.268	3.27	1.39	61
	inclined	226.740	2.33	1.39	25
Substituted	Pt-Cu (f-step)	87.802	3.29 (S-Pt)	1.39	44
	Rh-Cu (f-step)	137.01	3.18 (S-Rh)	1.39	39

a The *C-C* bond length in the gas phase is 1.38 Å.
b The tilt angle between the molecule plane and the surface plane is θ.

S mode adsorption with the edge of MoS_2. This behavior is in good agreement with our present results where the adsorption modes of thiophene are modified when going from a perfect to a stepped Cu (100) surface. As detailed geometry in this adsorption configuration, the thiophene molecule binds to the surface through both the sulfur and the aromatic ring, with S —— Cu and ring — Cu distances of 2.40 Å and 3.23 Å, respectively. Here, bond distances C —— C show no significant stretching with a distance of 1.38 Å and an inclination angle of 22° from the surface.

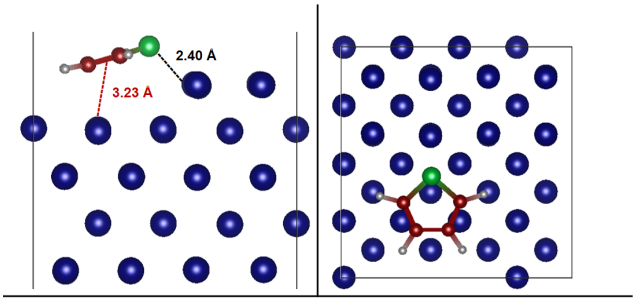

Fig. 2 Side and top views of thiophene adsorbed on the most stable configuration (flat-lower terrace). Blue, green, grey, and dark red balls represent copper, sulfur, hydrogen, and carbon atoms, respectively. The values illustrated in the Figure indicate the shorter S−Cu (black) and ring−Cu (red) distances, respectively.

To gain insights into the impact of weakly coordinated atoms (stepped atoms) on the adsorption behavior of the thiophene molecule, we replaced the Cu atoms in the stepped layer with Pt or Rh atoms (**Figure 3**). Initially, we shifted the preferred thiophene configuration from a flat lower terrace arrangement to a flat step configuration for both cases—Pt-Cu and Rh-Cu. The total interaction energies for these configurations were measured at 87.802 kJ/mol (Pt-Cu) and 137.01 kJ/mol (Rh-Cu), both of which were lower than the energies associated with the stepped Cu terrace. This adsorption pattern primarily arises from π interactions, where the thiophene ring approaches the Pt and Rh atoms at distances of 2.46 Å and 2.31 Å , respectively. Notably, the S —— Pt and S —— Rh bond lengths are 3.18 Å and 3.29 Å , respectively. However, 85% (75.01 kJ/mol) and 51% (69.29 kJ/mol) of the total interaction energy corresponds to dispersion energy for Pt-Cu and Rh-Cu surfaces, respectively. This higher energy component corresponds to physisorption, lacking significant chemical interaction or dissociative adsorption. This indicates a higher sensing capability with good regenerability of these materials towards the thiophene molecule. Furthermore, these configurations indicate reduced interaction between thiophene and the Cu atoms of the second layer. Drawing parallels with benzene as a thiophene-like structure, earlier research on benzene adsorption onto a Pt (221) step surface reveals that the most stable sites are situated at the step edges[43].

3.1.2 Adsorption of pyridine

Table 2 summarizes the energy and geometrical details of the pyridine molecule on different surfaces. The flat-lower terrace as the stable adsorption configuration of the pyridine molecule on the stepped surface of Cu (100) controlled by both π-interaction and N —— C interaction with a total interaction energy of 145.693 kJ/mol, see **Figure 4**. Inclined configurations are also interesting with total interaction energies of 144.73 kJ/mol, see SI for more details on all configurations tested. Whereas, on a perfect Cu (100) surface, the pyridine molecule has a vertical configuration with a total energy of 103.239 kJ/mol and an N —— Cu distance of 2.04 Å, which is less than its adsorption on a stepped surface by about 42 kJ/mol. In the same context,

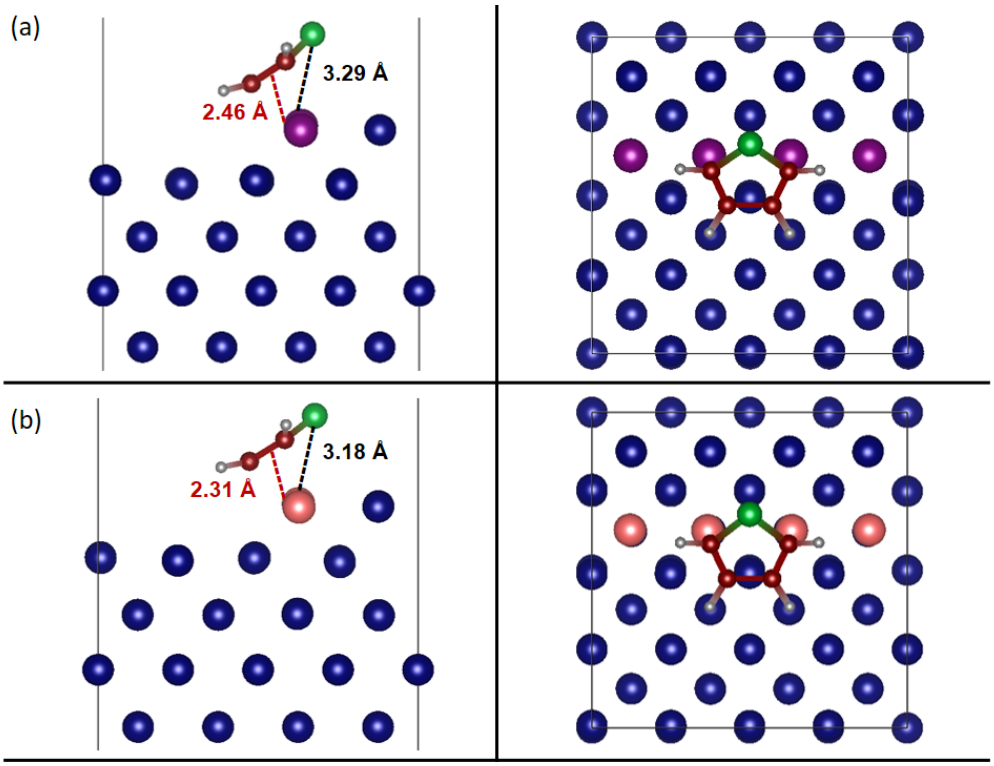

Fig. 3 Side and top views of thiophene adsorbed on the most stable configuration (flat-step). Blue, green, grey, purple, pink, and dark red balls represent copper, sulfur, hydrogen, platinum, rhodium, and carbon atoms, respectively. (a) and (b): Thiophene adsorbed on Pt-Cu and Rh-Cu substituted surface respectively. The values illustrated in the Figure indicate the shorter S−Pt/Rh (black) and ring−Pt/Rh (red) distances, respectively.

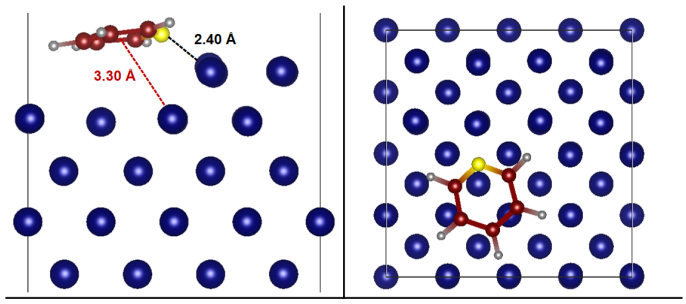

Fig. 4 Side and top views of pyridine adsorbed on the most stable configuration (flat-lower terrace). Blue, yellow, grey, and dark red balls represent copper, nitrogen, hydrogen, and carbon atoms, respectively. The values illustrated in the Figure indicate the shorter N−Cu (black) and ring−Cu (red) distances, respectively.

a previous study of the adsorption of pyridine on a perfect metal surface revealed that the N atom of pyridine adsorbs on top of a metal atom[25,74,75] which lined up with a good agreement to our study. The most sorbent configuration on a stepped Cu (100) surface represents the same behaviour provided by a perfect Cu (100) surface, where the nitrogen atom only binds to the neighboring Cu atom over a distance of 2.04 Å. Within the same framework, Tafreshi et al.[44] studied the adsorption of hydrazine on the perfect and defective copper surfaces (100), (110), and (111), and they found that the hydrazine molecule adsorbs through a nitrogen atom on the adatom Cu (100) and the vacancy Cu (100) and (110) surfaces. Moreover, Waldmann et al.[76] studied the adsorption of the pyridine molecule and large pyridine derivative molecules on a stepped Ag (100) surface, and they concluded that the hetero-cyclic nitrogen atoms in pyridine and their derivatives prefer the positions on top of Ag atoms.

As thiophene, pyridine was also adsorbed on a substituted Pt/Rh-Cu (100) stepped surface, see **Figure 5**. The total interaction energies of the pyridine molecule on Pt-Cu and Rh-Cu surfaces are 210.34 kJ/mol with a distance N−Pt of 2.18 Å and 198.76 kJ/mol with a distance N−Rh of 2.06 Å, respectively (see **Table 2**). An increase in total interaction energy is observed when moving from Cu to Pt-Cu and Rh-Cu stepped surfaces, which refers to changes in adsorption modes ranging from flat-lower terrace to inclined configuration. However, the distances between the pyridine ring and the metal atoms remained larger than 3 Å, showing a low π interaction between pyridine and metals.

3.1.3 Regeneration capacity

The bond lengths S——C and N——C are calculated in order to estimate the regeneration capacity of different surfaces, see **Table 3**. In short words, regenerative surfaces is a term used to describe the surfaces which are able to adsorb an adsorbent without undergoing molecular dissociation which might result in the formation of surface new radicals and therefore modifying its chemical composition[23]. Here, we compared the bond length of thiophene (S——C) and pyridine (N——C) in the gas phase and adsorbed on different surfaces while a large significant increase can lead to dissociation of molecules leading us to conclude that the corresponding surface is less regenerable.

Table 3 Bond length difference between the gas phase (before adsorption) and the complex phase (after adsorption) of thiophene (C_4H_4S) and pyridine (C_5H_5N) molecules.

Sorbent system	$\Delta(S-C_3)/\Delta(S-C_4)$ (Å)	$\Delta(N-C_5)/\Delta(N-C_4)$ (Å)
Cu	0.015/0.016	0.014/0.013
Pt-Cu	0.021/0.021	0.014/0.012
Rh-Cu	0.024/0.024	0.043/0.016

For both molecules, we can see that the interaction with each surface distinctly affects the heterogeneous intra-molecular distances. Considering the thiophene molecule, on Cu, Pt-Cu and Rh-Cu, both S——C bonds are elongated insignificantly by almost 0.016 Å, 0.021 Å, and 0.024 Å compared to those in the gas phase. Regarding the pyridine molecule, in Cu and Pt-Cu, the elongation of the two N——C bonds fell in the range between 0.012 Å and 0.014 Å, which can also be considered insufficient to promote dissociation of the pyridine molecule. Contrariwise, in Rh-Cu, one N——C bond was lengthened by around 0.043 Å while the second one was by 0.016 Å. Large elongation of one N——C bond by more than 0.03 Å could lead to the trap of the N atom in the adsorption site; thus, the dissociation of the pyridine molecule. In general, excluding the Rh-Cu/C_5H_5N system, no significant variation in bond lengths between the isolated molecules and after adsorption (< 0.03 Å) can lead to the dissociation of both molecules.

3.1.4 Water-inhibiting effect

In order to show the inhibiting effect of water on the processes of desulfurization and denitrogenation by Cu (100) surfaces, we study the adsorption of water on the stepped Cu, Pt-Cu, and Rh-Cu surfaces. The most stable adsorption configurations of water are shown in **Figure 7**. We can see that on any surface, the H_2O molecule prefers to be adsorbed on the metal atoms by its oxygen atom. The

Table 2 Geometries and total interaction energies (E_{int}) of the relaxed pyridine (C_5H_5N) adsorbed structures on perfect, stepped, and substituted Cu (100) Surface with Pt and Rh atoms.

Sorbent	Adsorption site	E_{int} (C_5H_5N) (kJ/mol)	N−Cu (Å)	C−C[a] (Å)	θ[b] (deg)
Perfect	Top	103.239	2.04	1.39	90
Stepped	v-upper terrace	101.31	2.04	1.39	90
	v-lower terrace	115.78	2.06	1.39	90
	f-lower terrace	145.693	2.04	1.39	14
	f-step	118.677	1.98	1.39	67
	inclined	144.73	2.04	1.39	4
Substituted	Pt-Cu (inclined)	210.34	2.18 (N-Pt)	1.39	13
	Rh-Cu (inclined)	198.76	2.06 (N-Rh)	1.40	20

[a] The C−C bond length in the gas phase is 1.39 Å.
[b] The tilt angle between the molecule plane and the surface plane is θ.

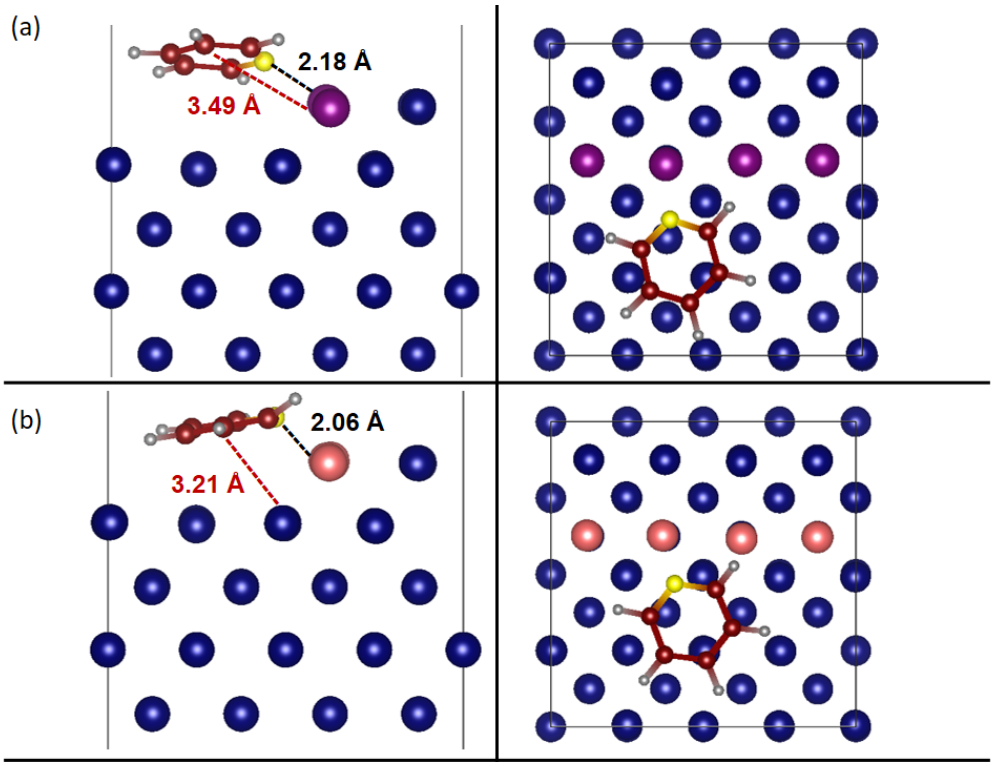

Fig. 5 Side and top views of pyridine adsorbed on the most stable configuration (inclined). Blue, yellow, grey, purple, pink, and dark red balls represent copper, nitrogen, hydrogen, platinum, rhodium, and carbon atoms, respectively. (a) and (b): Pyridine adsorbed on Pt-Cu and Rh-Cu substituted surface respectively. The values illustrated in the Figure indicate the shorter N−Pt/Rh (black) and ring−Cu/Pt/Rh distances, respectively.

total interaction energy of water is 44.38 kJ/mol on Cu, 27.98 kJ/mol on Pt-Cu and 46.31 kJ/mol on Rh-Cu (see **Figure 7**). In the case of Cu, Pt-Cu, and Rh-Cu surfaces, the smallest M-O distance between the metallic Cu/Pt/Rh atoms and the water O atom is 2.18/2.53/2.36 Å, respectively. This increase can be correlated with increases in atomic radius from Cu to Pt. It is clear that the highest energy is obtained with Rh-Cu, while the lowest is shown with Pt-Cu. Based on these findings, Rh-Cu should adsorb water more efficiently than Cu and Pt-Cu. However, likewise on all surfaces studied in here, the total interaction energies of the water molecule are low, meaning that physisorption might be mainly controling its adsorption mechanisms. Evaluating the adsorption of water in comparison to that of thiophene or pyridine, we found out that the latter molecules are more highly absorbed than water on any surface considered meaning that there is no inhibiting effect of water on any of desulfurization and denitrogenation processes, see **Figure 6**.

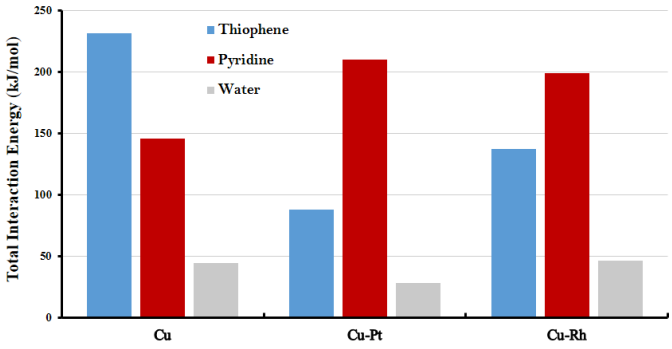

Fig. 6 Variation of the total interaction energy (kJ/mol) of thiophene, pyridine and water depending on the sorbent Cu, Pt-Cu and Rh-Cu stepped terraces.

3.2 Exploring Molecular Dynamics Simulations

To thoroughly explore how temperature affects the efficiency of the Cu surface to facilitate desulfurization and denitrogenation processes, molecular dynamics simulations were performed based on the reax force field, which is known to accurately represent molecular interactions thanks to its consideration of bond order and reactivity. Our investigation mainly focused on the analysis of interactions involving thiophene and pyridine molecules. This analysis delved into the specific behaviors of these molecules when they come into contact with a Cu surface at room temperature (300 K). We extended our exploration to include scenarios where a mixture of these molecules interacted with the Cu surface. This allowed us to better understand the complex interaction between thiophene, pyridine and the Cu surface. An important part of our study was devoted to evaluate how water molecules influence the adsorption dynamics of these mixed molecules. Our intention in introducing water into the system was to find out how its presence affects the adsorption characteristics of thiophene and pyridine, potentially leading to changes in their usual adsorption behaviors.

In the absence of water molecules, the adsorption of thiophene and pyridine is primarily governed by the interactions of their sulfur and nitrogen atoms with the copper atoms on the surface, as depicted in **Figure 8(a-b)**. Interestingly, these adsorptions occur in a vertical orientation, which contrast with isolated adsorption modes where thiophene and pyridine prefer flat adsorption modes based on DFT calculations. This change in adsorption orientation can be attributed to competitive adsorption between the molecules, leading to repulsive interactions and causing them to adsorb vertically. Specifically, all thiophene molecules are adsorbed through their sulfur atoms at distances ranging from 2.10 to 2.41 Å from the nearest copper atoms, consistent with the S-Cu distances observed in DFT investigations. Moreover, 60% of these thiophene molecules are adsorbed behind the stepped region. In contrast, only 17% of pyridine molecules are directly adsorbed on copper atoms, while 8% adsorb on Cu step region with an N-Cu distance of 2.10 Å. The remaining pyridine molecules are situated much farther away, at distances greater than 4 Å from the surface.

In the presence of water molecules, as shown in **Figure 8(c-d)**, the adsorption behavior of thiophene and pyridine on the clean Cu (100) stepped surface was altered. Approximately 75% of thiophene molecules were adsorbed on the upper terrace of the surface, with 60% of these molecules approaching step atoms, and the smallest S-Cu distance was about 2.17 Å . Moreover, 50% of the pyridine molecules were positioned at N-Cu distances of approximately 3 Å. The remaining molecules of both thiophene and pyridine were not adsorbed and remained distant from the surface. The water molecules spread across the entire surface, with most of them being located near the pyridine molecules. This distribution suggests that water molecules may have an affinity for or preferential interaction with the pyridine adsorbates on the surface.

Regarding the desulfurization and denitrogenation processes, these MD simulations showed more promising results compared to previous DFT calculations. In the

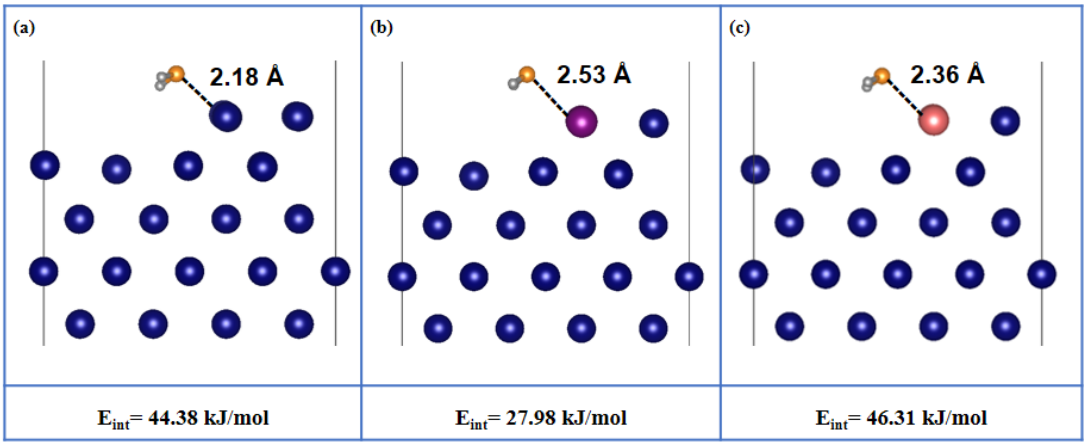

Fig. 7 The most stable adsorption configurations were calculated for water (H2O) over (a) Cu, (b) Pt-Cu, and (c) Rh-Cu stepped surfaces. Blue atoms correspond to Cu atoms, purple atoms correspond to Pt atoms, pink atoms correspond to Rh atoms, orange atom correspond to O atom and grey atoms correspond to H atoms.

absence of water molecules, approximately 1% of thiophene exhibited a single S-C bond cleavage, resulting in an elongation of the S —— C bond distance to 1.87 Å. For 45% of thiophene molecules, two S —— C bonds were broken, with 30% of them displaying S —— C bond distances of 1.9 Å and the remaining 15% showing bond distances exceeding 1.98 Å. Interestingly, the last 10% of thiophenes were adsorbed on Hollow sites, experiencing complete deformation and dissociation. In contrast, only a minimal elongation of 0.05 Å was observed for certain intramolecular N —— C bonds of pyridine.

The heterogeneous intramolecular bonds S —— C and N —— C were also affected in the presence of water molecules. Among the adsorbed thiophene molecules, as presented in **Figure 8-e**, 10% exhibited one S —— C cleavage, with the bond length exceeding 1.9 Å, while 90% experienced the breaking of two S —— C bonds at lengths greater than 1.9 Å. As for the adsorbed pyridine (see **Figure 8-f**), 70% of both N —— C bonds were dissociated, with bond distances exceeding 1.5 Å. In the same context, 90% of the adsorbed water molecules underwent dissociation to form separate entities: hydrogen (H) and hydroxyl (OH) radicals, while only 10% of water molecules remained unchanged (see **Figure S6**). These hydrogen radicals strongly attracted the majority of the separate N atoms, with the smallest H-N distance being 1.1 Å. Conversely, the dissociated S atoms were separated by more than 3 Å from the nearest H radical. The interaction between pyridine molecules and water molecules may lead to the challenging adsorption of pyridine molecules on the surface and hinder the denitrogenation process.

Overall, the results presented in this section confirm the higher affinity of the clean Cu (100) stepped surface to adsorb and remove sulfur and/or nitrogen compounds, with a particular favorability towards the desulfurization process, consistent with DFT results, especially in a non-humid environment.

In order to determine the average distance between the Cu stepped surface and various adsorbates, we conducted partial radial distribution function (RDF) analyses. The results of our investigation are presented in **Figure 9**, which displays the RDFs of Cu–N, Cu–S, and Cu–O_{H_2O}. In the case of thiophene, the Cu-S peak is situated at 2.23 Å, both with and without water molecules. Notably, this observed Cu-S distance at the Cu-thiophene interface aligns with the range of distances obtained from DFT calculations (from 2.27 Å to 2.42 Å). For Cu–O_{H_2O} RDF, the peak appears at 1.93 Å , representing the scenario where a Cu atom is attracted to a water molecule. In this context, the oxygen atom of the water molecule binds to the Cu atom due to its closer proximity to the Cu surface. In the Cu–N RDF, in the absence of water molecules, the peak is evident at 1.93 Å . These observations are consistent with DFT findings of the Cu-pyridine interface, where the Cu-N distance extends from 1.98 Å to 2.04 Å. Conversely, in the presence of water molecules, no peak emerges at distances less than 3 Å, indicating a lack of interactions between Cu and N atoms. Therefore, the presence of water molecules appears to inhibit pyridine adsorption and suppress the denitrogenation process.

On the one hand, to examine the behavior of pyridine and thiophene adsorption on the Cu (100) surface,

we utilized potential of mean force (PMF) calculations at 300 K to derive the potential energy surface. We tracked the reaction coordinate from the gas phase to the surface. In this study, we compared the nature of the surface, including both defective (stepped) and perfect ones, for both thiophene and pyridine molecules. On the other hand, we investigated the competitive adsorption between these two molecules on their respective surfaces. Figure 10(a-b) shows that the adsorption of thiophene via its S atom on the perfect region requires a barrier energy of about 0.52 eV for the transition from the gas phase to the adsorption configuration state at 4.5 Å to the final state at 2.23 Å, compared to 0.38 eV for its adsorption on the stepped region. This indicates that adsorption on the stepped region, which requires a lower barrier energy, is more favorable. The same behavior is observed in the case of pyridine adsorption, where on the perfect surface, pyridine adsorption from the gas phase requires a barrier energy of 0.89 eV to be adsorbed on the Cu surface, ranging from 4.5 Å to 1.93 Å. While this barrier energy decreases to 0.53 eV for adsorption on the stepped region as indicated in Figure 10. Whether on the perfect region or the stepped one, the PMF calculations reveal that thiophene requires a lower barrier energy than pyridine to be adsorbed. This confirms, as demonstrated below, that thiophene prevails in the competitive adsorption.

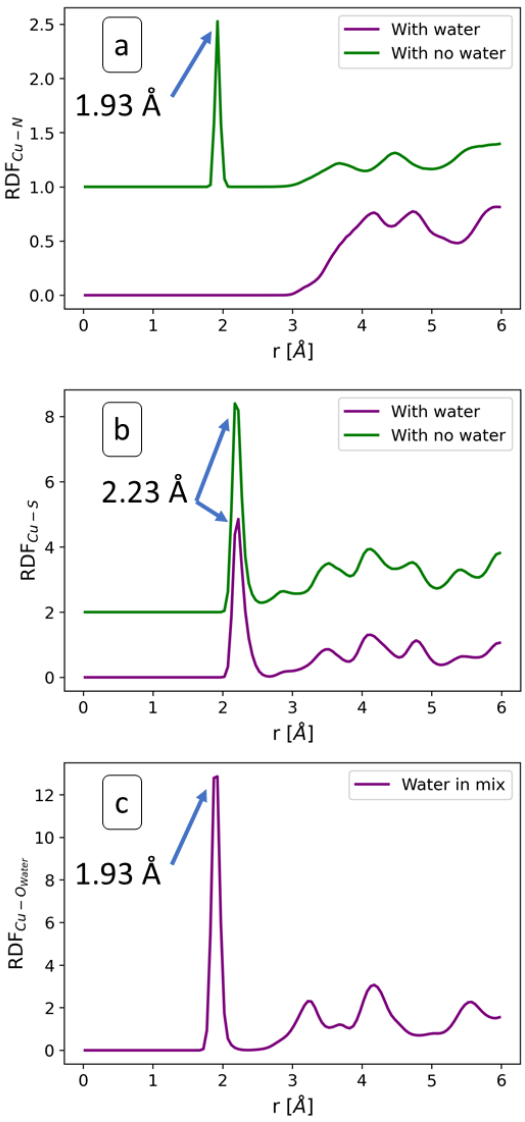

Fig. 9 Partial radial distribution functions (RDFs) for (a) Cu–N, (b) Cu–S, and (c) Cu–O_{H_2O} interactions at the (thiophene & pyridine)–Cu (100) interface, both in the absence and presence of water. The RDFs were calculated based on the data from the final 0.5 ns of the NVT simulation at 300 K.

4 Discussion

After analysis of the adsorption results (**Figure 6**), on the stepped surface of Cu (100), thiophene is adsorbed more strongly than pyridine at about 86 kJ/mol, showing higher affinity towards thiophene than pyridine. Thus, we have come to conclude that Cu surfaces could be used to selectively adsorb thiophene from a mixture containing thiophene and pyridine altogether, in other words, Cu surfaces are found to be more suited to the desulfurization process than to the denitrogenation process. However, the total in-

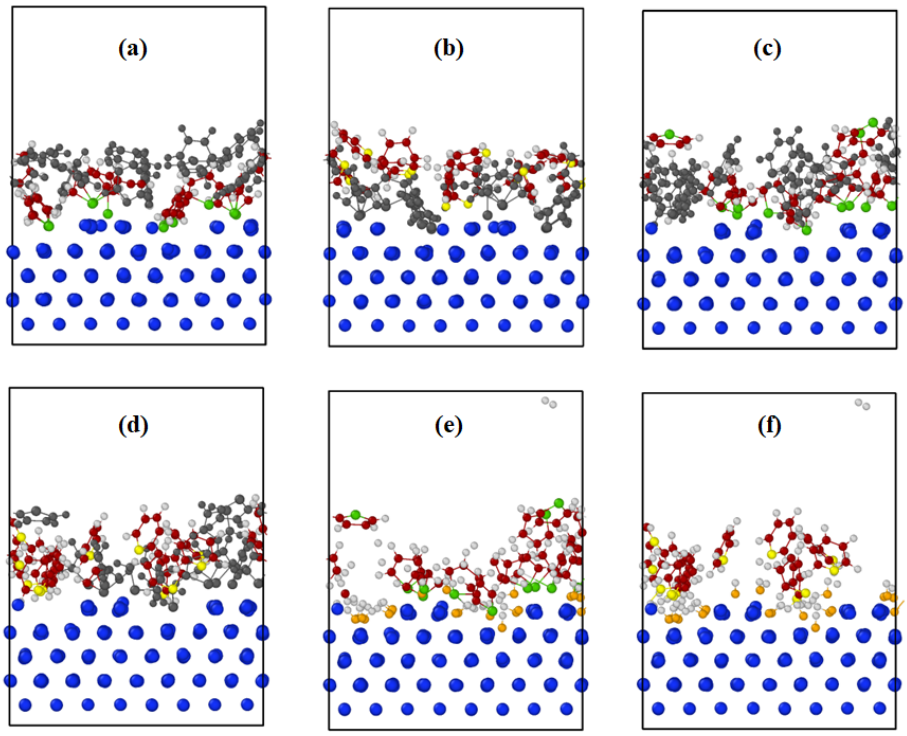

Fig. 8 Competitive adsorption between thiophene and pyridine is depicted, emphasizing the preference of thiophene, highlighted in its designated color, as shown in (a) without and (c) with water molecules, while pyridine is represented as a secondary structure in dark color. Conversely, pyridine is highlighted with its color code in (b) without and (d) with water molecules, with thiophene as a secondary structure in dark color. The adsorption of thiophene (e) and pyridine (f) is illustrated in the presence of water molecules. In this representation, blue, green, white, yellow, orange, and dark red spheres correspond to Cu, S, H, N, O, and C atoms, respectively.

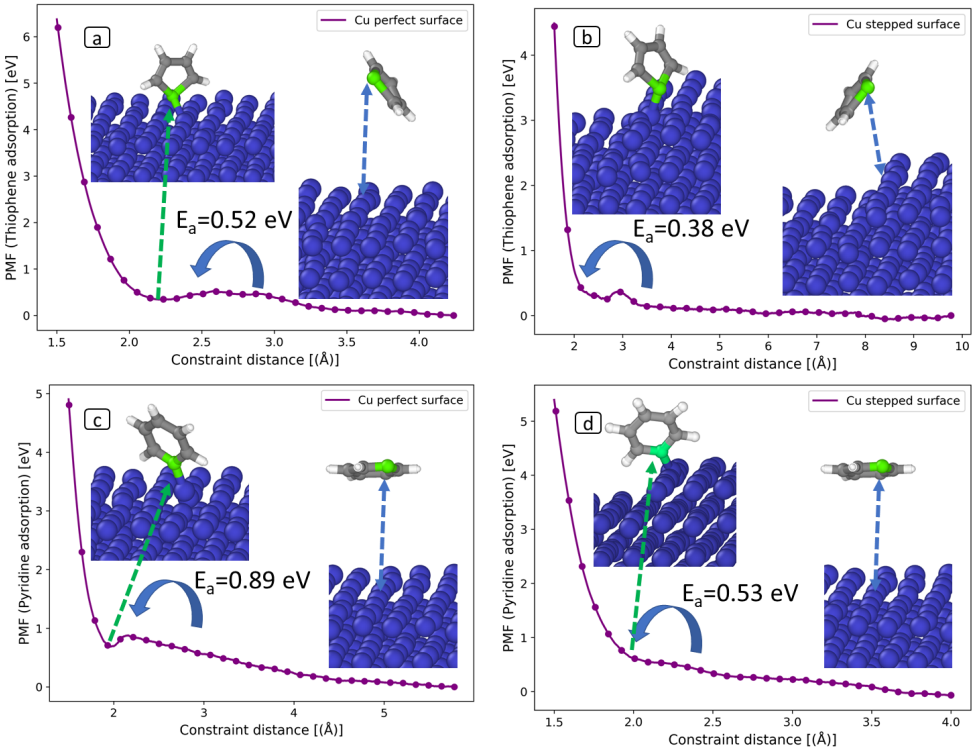

Fig. 10 Potential of Mean Force (PMF) energies at 300 K for adsorption pathways and the corresponding barrier energies for thiophene on a perfect Cu (100) surface (a) and a stepped Cu (100) surface (b), and for adsorption pathways of pyridine on a perfect Cu (100) surface (c) and a stepped Cu (100) surface (d).

teraction energy of thiophene on Cu is too high (231.565 kJ/mol), which could inhibit the process of desorption. In the case of Pt-Cu and Rh-Cu subsurfaces, thiophene is less adsorbed than pyridine by 122.54 and 61.75 kJ/mol, respectively, exhibiting higher affinity for pyridine than for thiophene. This could mean that Pt-Cu and Rh-Cu subsurfaces could be more favourable to the denitrogenation process than desulfurization. Regarding the regeneration capacity of the sorbents, with the exception of the Rh-Cu surface for the adsorption of pyridine, all the other surfaces tested are regenerable and can be used in complete safety for the desulfurization and denitrogenation processes. In terms of water inhibiting effect, the systems examined can be ranked in ascending order as follows: Rh-Cu, Cu, and Pt-Cu are the best candidates for strong affinity towards thiophene and pyridine molecules in a humid environment. The adsorption mechanism of thiophene and pyridine molecules on a stepped Cu (100) surface is further explained by electronic analysis. Bader's charge investigation[77,78] was employed to calculate the electron transfer between the surfaces and molecules. An amount of positive charges is indicated when transferring electrons from the surface to the molecule. As shown in **Table 4**, thiophene molecule receives a small amount of charge in the cases of perfect Cu and stepped Rh-Cu substrate, while for the other substrates the direction of electron transfer gets reversed. In the case of the pyridine molecule, the charge transfer mechanism of the pyridine molecule, on the substituted surfaces, was almost similar to the mechanism of thiophene. On the perfect surface of Cu (100), electrons of about 0.07 are transferred from the pyridine molecule, while on stepped one, electrons of about 0.06 are received by the pyridine molecule. The highest electronic changes are observed for the Rh-Cu/C_5H_5N system. This small transfer of charges indicates the favouring of molecular bonding instead of ionic bonding. Overall, these electronic results are insufficient to properly describe the adsorption behaviour. In contrast, plotting the electron density difference was essential to identify the type of bond spanning the molecule/metal interactions. Here, we can observe from these profiles the validity of the geometric results. **Figure 11-a** shows a small accumulation of charge on the S-Cu region, while the S atom or its closest Cu atom shows a state of loss of charge, which promotes the S-Cu covalent bond. For the substituted surfaces, the behaviour has been changed and the electron density map shows a higher depletion charge around the C atoms and a charge accumulation between the Pt/Rh and C atoms (see **Figure 11-b/c**). This type of interaction could explain the decrease in the total interaction energy since aromatic molecules tend to

be suited in parallel to surfaces and interact only with their delocalized electrons.

The mechanism of adsorption of the pyridine molecule on clean and substituted surfaces behaves similarly, in which the pyridine molecule interacts via its hetero-N atom on the nearest metal atom, promoting covalent bonding/electrostatic interactions. In addition, charge accumulation in the N-metal region and depletion around N, Cu, Pt and Rh atoms were increased when switching from Cu surfaces to Pt-Cu and Rh-Cu surfaces[79]. The Rh-Cu electron density map shows a double contribution of Rh with N and a C atom, leading to a higher charge transfer to the pyridine molecule (+0.13 e-) which could help in its detection, see **Figure 11-f**.

To better understand the adsorption behaviour of molecules on different surfaces, the work function (ϕ) is also taken into account (**Table 5**). This physical quantity represents the minimum energy necessary to free an electron from a material. The work function of thiophene on a perfect or stepped Cu surface decreased by only 0.24 eV, while on Pt-Cu and Rh-Cu surfaces the work function decreased by 0.33 and 0.43 eV, respectively. This allows the electron to easily cross the potential barrier and facilitate the detection mechanism. This higher sensing capacity can be explained by the electronic and chemical sensitization effects of Pt and Rh on the Cu surface. The lower work function of Pt-Cu and Rh-Cu, compared to that of Cu, facilitates more electron transfer between these surfaces and C_4H_4S, resulting in an increased sensing response. In the same context, a previous experimental investigation on the sensor response of Pt decorated CuO nanorods, it was found that this material can be considered as an optimal sensor for some volatile organic compounds[35]. Compared to thiophene adsorption, the work function reduction after pyridine adsorption was less, showing only 0.24 and 0.30 eV decrease for Pt-Cu and Rh-Cu surfaces, respectively.

Table 4 Bader charge transfer obtained for thiophene (C_4H_4S) and pyridine (C_5H_5N) molecules.

Sorbent	Charge transfer to C_4H_4S (e-)	Charge transfer to C_5H_5N (e-)
Cu perfect (Adsorption site)	+0.08 (Hollow)	-0.07 (Top)
Cu (Adsorption site)	-0.003 (f-lower terrace)	+0.06 (f-lower terrace)
Pt-Cu (Adsorption site)	-0.08 (f-step)	-0.07 (inclined)
Rh-Cu (Adsorption site)	+0.07 (f-step)	+0.13 (inclined)

Table 5 The work function change ($\Delta\phi$) of thiophene and pyridine molecules adsorbed on perfect, stepped, and substituted Cu (100) surface. The work function value ϕ_0 of isolated Cu (100) surface is 4.909 eV.

Sorbent	Work function change ($\Delta\phi$) (eV) C_4H_4S	Work function change ($\Delta\phi$) (eV) C_5H_5N
Cu perfect	-0.24	-0.22
Cu	-0.24	-0.29
Pt-Cu	-0.33	-0.24
Rh-Cu	-0.43	-0.30

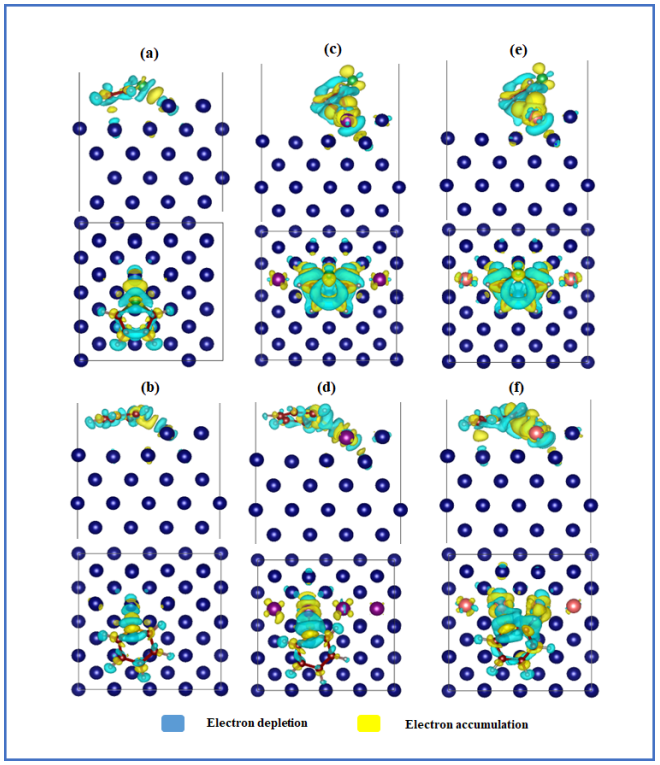

Fig. 11 The difference in electron ($\Delta\rho$) induced by the adsorption of thiophene and pyridine in Cu ((a) and (b)), Pt-Cu ((c) and (d)) and Rh-Cu ((e) and (f)) stepped terraces, respectively. Blue, green, grey, yellow, pink, purple, and dark red balls represent Cu, S, H, N, Rh, Pt and C atoms, respectively. The iso-value is ($2 \times 10^{-3} e/\text{Å}^3$).

5 Conclusion

In this study, we employed DFT calculations to evaluate the adsorption behavior of thiophene and pyridine molecules on both the pristine and Pt/Rh-doped Cu (100) stepped surface. Our main findings are summarized as follows:

- On the pristine surface, thiophene and pyridine molecules are adsorbed onto a level lower terrace through sulfur and nitrogen bindings, respectively.

- On doped surfaces, the adsorption pattern of thiophene shifts from a flat lower terrace to a flat step, enhancing Pt/Rh-aromatic ring interactions and significantly lowering energy levels.
- On doped surfaces, pyridine assumes a tilted configuration upon adsorption, demonstrating interactions involving both nitrogen and subtle π-bonds with the surface, resulting in strong adsorption.
- The overall interaction energy of thiophene follows this order on surfaces: Pt-Cu $<$ Rh-Cu $<$ Cu. For pyridine, the sequence is Cu $<$ Rh-Cu $<$ Pt-Cu.
- Bader's analysis revealed minor charge transfers between the molecules and the surfaces, indicating the prevalence of molecular bonds over ionic bonds. This observation is further supported by electron density difference plots.
- The physisorption behavior of thiophene, along with a substantial reduction in work function values for Pt-Cu and Rh-Cu materials, indicates a good sensing capacity towards the thiophene molecule.
- MD simulations show that pyridine and thiophene molecules are adsorbed vertically via their N and S atoms, respectively.
- In a non-humid environment, MD simulations highlight the predominance of thiophene molecules in the competitive adsorption process, with the amount of adsorbed thiophene and pyridine molecules reaching 100% and 17% of their initial amounts, respectively.
- In a humid environment, 75% of the thiophene molecules were adsorbed onto the Cu surface.
- MD results show that the presence of water molecules hampers the adsorption of pyridine and curtails the denitrogenation process.
- PMF calculations show that the adsorption pathway of thiophene, whether on the stepped or perfect region of the Cu (100) surface, requires a lower barrier energy than pyridine.

To summarize the preference of adsorption, we found that the Cu (100) stepped surface exhibits a stronger inclination towards thiophene compared to pyridine. In contrast, Pt-Cu and Rh-Cu surfaces exhibit higher pyridine adsorption compared to thiophene, with pyridine being notably more favored on the Rh-Cu surface by approximately 62 kJ/mol. This highlights the superior detection capability of pyridine over thiophene. As for regenerability, our investigation suggests that nearly all studied surfaces possess a significant capacity for regeneration. We anticipate that our study will inspire further theoretical and experimental endeavors in the realm of novel sorbents for processes involving desulfurization and denitrogenation.

Author Contributions

All authors contributed equally in this work.

Conflicts of interest

All authors confirm that there are no financial conflicts of interest or personal relationships that could impede the publication of the study discussed in this article.

Acknowledgements

We extend our gratitude to the Moroccan Ministry of Higher Education, Scientific Research, and Innovation, as well as the OCP Foundation, for their generous funding of this project through the APRD research program. Additionally, we acknowledge the utilization of computing resources from CALMIP in the execution of this work.

References

1 S. T. Oyama, *Journal of catalysis*, 2003, **216**, 343–352.
2 I. Babich and J. Moulijn, *Fuel*, 2003, **82**, 607–631.
3 C. A. Classa, J. Aguilera-Iparraguirrea and W. H. Greena.
4 R. T. Yang, *Adsorbents: fundamentals and applications*, John Wiley & Sons, 2003.
5 C. Song and X. Ma, *Applied Catalysis B: Environmental*, 2003, **41**, 207–238.
6 X. Ma, S. Velu, J. H. Kim and C. Song, *Applied Catalysis B: Environmental*, 2005, **56**, 137–147.
7 L. Duan, X. Gao, X. Meng, H. Zhang, Q. Wang, Y. Qin, X. Zhang and L. Song, *The Journal of Physical Chemistry C*, 2012, **116**, 25748–25756.
8 J. Weitkamp, M. Schwark and S. Ernst, *Journal of the Chemical Society, Chemical Communications*, 1991, 1133–1134.
9 A. J. Hernández-Maldonado and R. T. Yang, *Journal of the American Chemical Society*, 2004, **126**, 992–993.
10 B. Chawla, *Journal of Chromatographic Science*, 1997, **35**, 97–104.
11 J. Wen, X. Han, H. Lin, Y. Zheng and W. Chu, *Chemical*

Engineering Journal, 2010, **164**, 29–36.
12 K. Thomas, I. Khalil and F. Maugé, 8th Serbian-Croatian-Slovenian Symposium on Zeolites, 2019, p. 41.
13 L. Alaerts, C. E. Kirschhock, M. Maes, M. A. Van Der Veen, V. Finsy, A. Depla, J. A. Martens, G. V. Baron, P. A. Jacobs, J. F. Denayer *et al.*, *Angewandte Chemie International Edition*, 2007, **46**, 4293–4297.
14 J. H. Kim, X. Ma, A. Zhou and C. Song, *Catalysis Today*, 2006, **111**, 74–83.
15 R. T. Yang, A. J. Hernández-Maldonado and F. H. Yang, *Science*, 2003, **301**, 79–81.
16 X. Ma, M. Sprague and C. Song, *Industrial & Engineering Chemistry Research*, 2005, **44**, 5768–5775.
17 A. Srivastav and V. C. Srivastava, *Journal of hazardous materials*, 2009, **170**, 1133–1140.
18 R. Dehghan and M. Anbia, *Fuel Processing Technology*, 2017, **167**, 99–116.
19 F. Tian, X. Sun, X. Liu, H. Zhang, J. Liu, H. Guo, Y. Zhang and C. Meng, *Chinese Journal of Chemical Engineering*, 2020, **28**, 414–419.
20 A. S. Hussain and B. J. Tatarchuk, *Fuel*, 2013, **107**, 465–473.
21 B. Van de Voorde, M. Hezinová, J. Lannoeye, A. Vandekerkhove, B. Marszalek, B. Gil, I. Beurroies, P. Nachtigallb and D. De Vosa.
22 A. J. Hernández-Maldonado, S. D. Stamatis, R. T. Yang, A. Z. He and W. Cannella, *Industrial & Engineering Chemistry Research*, 2004, **43**, 769–776.
23 E. P. Hessou, H. Jabraoui, I. Khalil, M.-A. Dziurla and M. Badawi, *Applied Surface Science*, 2021, **541**, 148515.
24 M. Vuorte, S. Kuitunen and M. Sammalkorpi, *Physical Chemistry Chemical Physics*, 2021, **23**, 21840–21851.
25 W. Malone, J. von der Heyde and A. Kara, *The Journal of Chemical Physics*, 2018, **149**, 214703.
26 S. Moussadeq, M. Jabrane, A. Benbella, I. Matrane, M. Badawi, S. Lebègue, A. Kara and M. Mazroui, *Surface Science*, 2023, **734**, 122321.
27 R. T. Yang, A. Takahashi and F. H. Yang, *Industrial & Engineering Chemistry Research*, 2001, **40**, 6236–6239.
28 X. Han, H. Li, H. Huang, L. Zhao, L. Cao, Y. Wang, J. Gao and C. Xu, *RSC advances*, 2016, **6**, 75006–75013.
29 H. Li, X. Han, H. Huang, Y. Wang, L. Zhao, L. Cao, B. Shen, J. Gao and C. Xu, *Journal of colloid and interface science*, 2016, **483**, 102–108.
30 Y. Qin, Z. Mo, W. Yu, S. Dong, L. Duan, X. Gao and L. Song, *Applied surface science*, 2014, **292**, 5–15.
31 O. Marchenko and J. Cousty, *Physical Review Letters*, 2000, **84**, 5363.
32 M. Furukawa, H. Tanaka, K.-i. Sugiura, Y. Sakata and T. Kawai, *Surface science*, 2000, **445**, L58–L63.
33 J. V. Barth, J. Weckesser, C. Cai, P. Günter, L. Bürgi, O. Jeandupeux and K. Kern, *Angewandte Chemie International Edition*, 2000, **39**, 1230–1234.
34 A. K. Boal, F. Ilhan, J. E. DeRouchey, T. Thurn-Albrecht, T. P. Russell and V. M. Rotello, *Nature*, 2000, **404**, 746–748.
35 N. Sarıca, O. Alev, L. Ç. Arslan and Z. Z. Öztürk, *Thin Solid Films*, 2019, **685**, 321–328.
36 W. Y. Chen, C.-C. Yen, S. Xue, H. Wang and L. A. Stanciu, *ACS applied materials & interfaces*, 2019, **11**, 34135–34143.
37 C.-T. Wang, Y.-F. Zhang and S. Du, *Surfaces*, 2021, **4**, 31–38.
38 R. E. Kelly, M. Lukas, L. N. Kantorovich, R. Otero, W. Xu, M. Mura, E. Lægsgaard, I. Stensgaard and F. Besenbacher, *The Journal of chemical physics*, 2008, **129**, 184707.
39 M. Mura, A. Gulans, T. Thonhauser and L. Kantorovich, *Physical Chemistry Chemical Physics*, 2010, **12**, 4759–4767.
40 H. Yildirim and A. Kara, *The Journal of Physical Chemistry C*, 2013, **117**, 2893–2902.
41 J. Matos, H. Yildirim and A. Kara, *The Journal of Physical Chemistry C*, 2015, **119**, 1886–1897.
42 Y. Jiang, J. Li, G. Su, N. Ferri, W. Liu and A. Tkatchenko, *Journal of Physics: Condensed Matter*, 2017, **29**, 204001.
43 K. Lakshmikanth, M. F. Puthiyaparambath, S. Anoop and R. Chatanathodi, *Surface Science*, 2022, **716**, 121959.
44 S. S. Tafreshi, A. Roldan and N. H. de Leeuw, *The Journal of Physical Chemistry C*, 2014, **118**, 26103–26114.
45 C. Morin, A. Eichler, R. Hirschl, P. Sautet and J. Hafner, *Surface science*, 2003, **540**, 474–490.
46 M. Gajdoš and J. Hafner, *Surface science*, 2005, **590**, 117–126.
47 L. Buimaga-Iarinca and C. Morari, *Theoretical Chemistry Accounts*, 2014, **133**, 1–11.
48 L. Buimaga-Iarinca and C. Morari, *RSC advances*, 2013, **3**, 5036–5044.
49 H. Jabraoui, A. Estève, S. Hong and C. Rossi, *Physical Chemistry Chemical Physics*, 2023, **25**, 11268–11277.
50 A. J. Marsden, M. Skilbeck, M. Healey, H. R. Thomas, M. Walker, R. S. Edwards, N. A. Garcia, F. Vuković, H. Jabraoui, T. R. Walsh *et al.*, *Physical Chemistry Chemical Physics*, 2022, **24**, 2318–2331.
51 H. Jabraoui, A. Esteve, M. Schoenitz, E. L. Dreizin and

C. Rossi, *ACS applied materials & interfaces*, 2022, **14**, 29451–29461.
52 J. Yeon, H. L. Adams, C. E. Junkermeier, A. C. Van Duin, W. T. Tysoe and A. Martini, *The Journal of Physical Chemistry B*, 2018, **122**, 888–896.
53 P. Losch, H. R. Joshi, O. Vozniuk, A. Grünert, C. Ochoa-Hernández, H. Jabraoui, M. Badawi and W. Schmidt, *Journal of the American Chemical Society*, 2018, **140**, 17790–17799.
54 G. Kresse and J. Furthmüller, *Computational materials science*, 1996, **6**, 15–50.
55 G. Kresse and J. Furthmüller, *Physical review B*, 1996, **54**, 11169.
56 P. E. Blöchl, *Physical review B*, 1994, **50**, 17953.
57 G. Kresse and D. Joubert, *Physical review b*, 1999, **59**, 1758.
58 J. P. Perdew, K. Burke and M. Ernzerhof, *Physical review letters*, 1996, **77**, 3865.
59 H. Jabraoui, M. Djafari Rouhani, C. Rossi and A. Esteve, *Phys. Rev. Mater.*, 2022, **6**, 096001.
60 H. Jabraoui, I. Khalil, S. Lebègue and M. Badawi, *Molecular Systems Design & Engineering*, 2019, **4**, 882–892.
61 H. Jabraoui, E. Hessou, S. Chibani, L. Cantrel, S. Lebègue and M. Badawi, *Applied Surface Science*, 2019, **485**, 56–63.
62 H. Jabraoui, T. Charpentier, S. Gin, J.-M. Delaye and R. Pollet, *The Journal of Physical Chemistry C*, 2021, **125**, 7919–7931.
63 A. Daouli, H. Jabraoui, B. Hartiti, A. Bouich, B. M. Soucase, E. Comini, H. M. M. Arachchige, S. Fadili, P. Thevenin, A. Kamal *et al.*, *Applied Surface Science*, 2022, **574**, 151585.
64 H. Jabraoui, T. Charpentier, S. Gin, J.-M. Delaye and R. Pollet, *The Journal of Chemical Physics*, 2022, **156**, 134501.
65 N. Ferri, R. A. DiStasio Jr, A. Ambrosetti, R. Car and A. Tkatchenko, *Physical review letters*, 2015, **114**, 176802.
66 S. Plimpton, *Journal of computational physics*, 1995, **117**, 1–19.
67 H. Jabraoui, S. Gin, T. Charpentier, R. Pollet and J.-M. Delaye, *The Journal of Physical Chemistry C*, 2021, **125**, 27170–27184.
68 D.-Y. Wu, B. Ren, Y.-X. Jiang, X. Xu and Z.-Q. Tian, *The Journal of Physical Chemistry A*, 2002, **106**, 9042–9052.
69 H. Orita and N. Itoh, *Surface Science*, 2004, **550**, 177–184.
70 S. Izrailev, S. Stepaniants, B. Isralewitz, D. Kosztin, H. Lu, F. Molnar, W. Wriggers and K. Schulten, Ideas, 1998, p. 39.
71 S. Park and K. Schulten, *The Journal of chemical physics*, 2004, **120**, 5946–5961.
72 C. Jarzynski, *Physical Review Letters*, 1997, **78**, 2690.
73 H. Jabraoui, C. Rossi, A. Alpuche and A. Esteve, *Available at SSRN 4553949*.
74 A. Bilić, J. R. Reimers and N. S. Hush, *The Journal of Physical Chemistry B*, 2002, **106**, 6740–6747.
75 K. Tonigold and A. Groß, *The Journal of chemical physics*, 2010, **132**, 224701.
76 T. Waldmann, C. Nenon, K. Tonigold, H. E. Hoster, A. Groß and R. J. Behm, *Physical Chemistry Chemical Physics*, 2012, **14**, 10726–10731.
77 R. F. Bader and M. E. Stephens, *Journal of the American Chemical Society*, 1975, **97**, 7391–7399.
78 R. F. Bader and C. F. Matta, *The Journal of Physical Chemistry A*, 2004, **108**, 8385–8394.
79 A. Benbella, I. Matrane, M. Badawi, S. Lebègue and M. Mazroui, *Surface Science*, 2023, **729**, 122212.